Supercomputer Windows into the Solar Convection Zone

Å. Nordlund

Theoretical Astrophysics Center, Juliane Maries vej 30, 2100 Copenhagen Ø, and
Astronomical Observatory / NBIfAFG, Juliane Maries vej 30, 2100 Copenhagen Ø

R. .F. Stein

Dept. of Phys. and Astronomy, Michigan State University, East Lancing


A. Brandenburg

NORDITA, Blegdamsvej 17, 2100 Copenhagen Ø, and
Dept. of Applied Mathematics, University of Newcastle

Abstract. We discuss the properties of convection in the solar convection zone(CZ), as revealed by supercomputer simulations. One class of models, covering roughly the first half of the logarithmic mass density interval from the photosphere to the bottom of the convection zone, is an accurate representation of the solar surface layers. These models provide quantitative information on the physically complicated top boundary layer, where fluctuation amplitudes are large, radiative energy transfer is important, and where the structure is crucial for both global solar structure and p-mode reflection properties. The second class of models are "toy models" that cover the second half of the logarithmic range in density and include the bulk and bottom CZ boundary, but whose parameters deviate in several ways from the actual solar CZ. These models are still able to provide a basis for discussions and speculations about the bottom boundary layer of the solar convection zone.

Key words: Convection, turbulence, solar convection zone

1. Introduction

Helioseismologic observations have opened observational windows into the interior of the Sun, and detections of p-modes in spectra of stars have opened up at least a tiny observational peep-hole into their interiors. In a complementary development, supercomputer
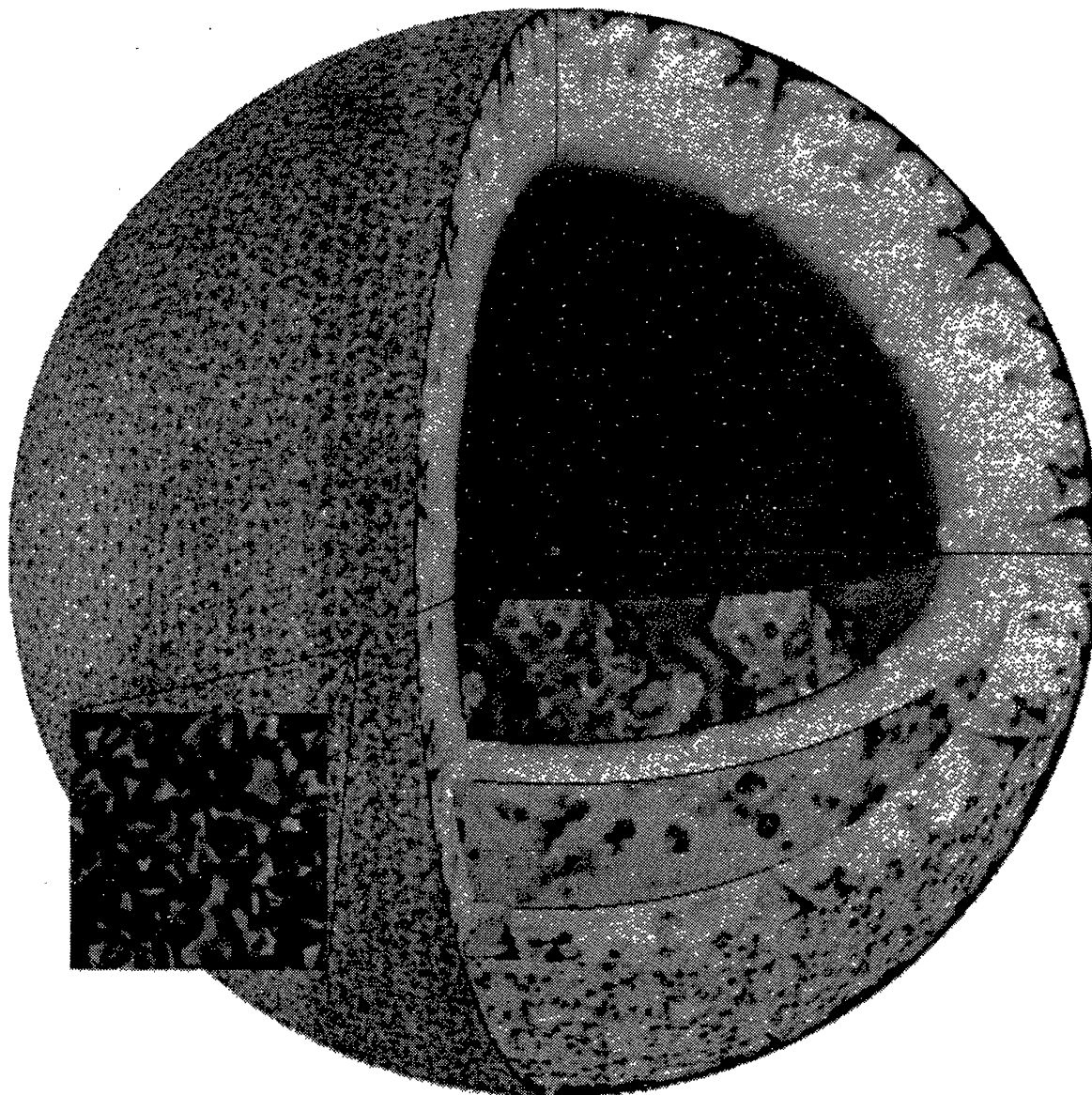
Figure 1. A composite illustration obtained by combining warped images from two simulations. One is a simulation of the near-surface region, using a realistic equation of state and a detailed treatment of radiative energy transfer, and the other is a "toy model" of the bulk of the convection zone that uses cartesian geometry and an ideal equation of state.

simulations have opened *virtual* windows into the solar and stellar interiors; using the results of supercomputer simulations, one may produce visualizations such as the one shown in Fig. 1.

The qualitative and quantitative information obtained from numerical simulations and subsequent visualizations can be quite suggestive, and may inspire new ways of looking at the phenomena under study. Indeed, numerical simulations have lead to a new picture of convection in strongly stratified media such as the solar convection zone

(Stein & Nordlund 1989, Spruit et al. 1990, Spruit 1996). Below we summarize our current understanding of solar convection.

We first (Section 2) discuss requirements on models of the solar convection zone, then (Section 3) discuss the solar surface layers, the bulk of the convection zone and the lower boundary layer (Section 4). Some concluding remarks are offered in Section 5.

2. Requirements on Numerical and Analytical Models

Stellar convection differs from laboratory convection in several fundamental ways; in particular the boundary layers are much more complex than the corresponding boundary layer in a laboratory experiment. The main complications are: 1) gravitational stratification, 2) penetrative boundaries, and 3) a very thin layer with radiative energy release within the upper boundary layer.

2.1. Gravitational stratification

One of the most fundamental properties of the solar convection zone is its enormous density contrast. Fig. 2 illustrates the density stratification, from the top of the photosphere to the bottom of the convection zone. Note that the mass density increases by over four orders of magnitude over the first 6 Mm, and then increases by another four orders of magnitude down to the bottom of the convection zone.
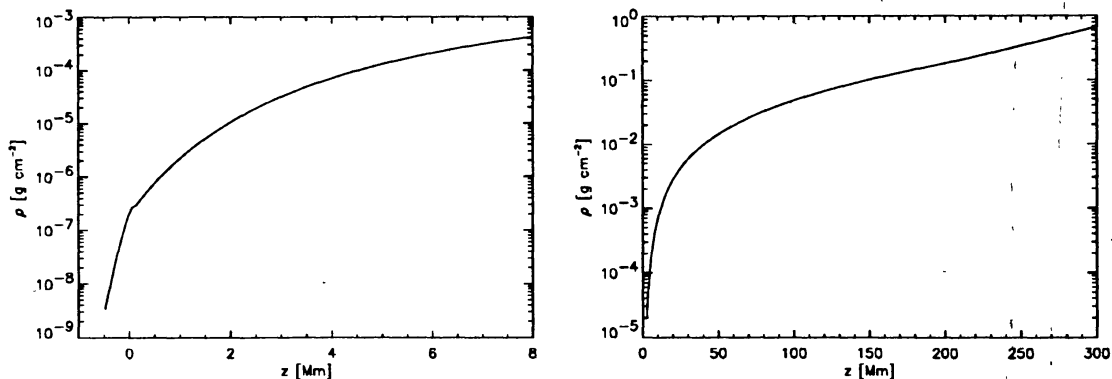
Figure 2. The solar mass density stratification, illustrated in two panels that each cover approximately half of the logarithmic interval in density, from the photosphere to the bottom of the convection zone.

There are two issues here: 1) the huge difference in mass density over scales comparable to a single convection cell; the energy carrying cells at the surface (granulation) have sizes of the order half the depth extent of Fig. 2a. 2) the differences in scale, that roughly follow the changes in scale heights in Fig. 2a-b; correspondingly, the turn-over times change from minutes at the top of the convection zone to weeks in the bulk of the convection zone.

The rapid variation of density over the scale of the flow is a challenge for numerical modeling, but one that can be handled. It is also a property that has a decisive influence on the character of the flow, and it is therefore worthwhile to briefly consider where and how the density stratification enters most decisively into the fluid equations.

The density changes are large in a Lagrangian frame (following the motion) as fluid moves up and down, but only moderate in the Eulerian frame of the numerical mesh, since the density at any one height is basically determined by hydrostatic equilibrium. Thus

$$\frac{D \ln \rho}{Dt} = -\nabla \cdot \mathbf{u} \tag{1}$$

is large, while

$$\frac{\partial \ln \rho}{\partial t} = -\frac{1}{\rho} \nabla \cdot (\rho \mathbf{u}) \tag{2}$$

is much smaller. The difference in the directional contributions to the right hand side divergences is mainly that in the latter case the vertical contribution roughly balances the sum of the two horizontal ones while in the first case there is a large net divergence or convergence. If we disregard the horizontal variation of density in comparison to the much larger vertical variation, we may conclude that

$$\frac{D \ln \rho}{Dt} \approx -u_z \frac{d \ln \langle \rho \rangle}{dz}, \tag{3}$$

where $\langle \rho \rangle$ is the horizontal (and time) average of the density. This just states that vertically moving fluid parcels must roughly follow the vertical variation of density, which is much larger than the horizontal fluctuations.

Thus, to a first approximation, all ascending fluid must expand, and all descending fluid must contract. The rates of expansion and contraction are large; a fluid parcel carrying thermal energy to the solar surface expands by a factor of more than one hundred over a vertical distance comparable to the horizontal cell size.

Similar considerations apply to the transport of entropy, for example; specific entropy is carried along with the flow, and any pattern of entropy fluctuations is subject to analogous Lagrangian expansion or contraction.

The approximate balance between vertical and horizontal mass flux divergence implied by Eq. (2) also explains why a particular range of cell sizes dominates the transport. If one ignores the vertical variation of the velocity, in comparison with that of the mass density, one obtains from a Fourier transform of Eq. (2) the estimate

$$U_{\text{horizontal}} \approx U_{\text{vertical}} \frac{\lambda_{horizontal}}{4\pi H_\rho}. \tag{4}$$

The amplitude of the vertical motion is basically determined by the amount of heat required to be transported to the surface, and hence Eq. (4) states that cells with larger horizontal size must have larger horizontal velocities, in order to provide the right amount

of horizontal velocity divergence. But the buoyancy driving that is available for accelerating the horizontal flow is set more or less by the amplitude of the temperature fluctuations, and these are almost independent of the horizontal size, since they are dominated by the thin surface layer, and non-local transport effects there. This produces horizontal velocity amplitudes comparable to the vertical ones, and hence Eq. (4) may be read as a constraint on the cell size, requiring the horizontal sizes of cells to be roughly one order of magnitude larger than the vertical scale heights, as is indeed the case with the solar granulation.

Thus, gravitational stratification introduces strong constraints on the fluid flow, and has a profound influence on the type of fluid motion patterns that can develop, as well as on their horizontal scales.

2.2. Radiative energy transfer

The energetically dominant pattern that we observe on the surface of the Sun is the granulation, with horizontal scales of order a Mm. Superficially, the pattern appears to be a familiar convection cell pattern; the bright granules correspond to ascending flows, and the dark lanes to descending flows. And yet, practically all motions that we can observe in the solar photosphere occur in a convectively stable layer; the mean entropy increases outwards throughout the visible parts of the photosphere, except for the first few tens of kilometers.

It is in this shallow layer, with an vertical extent roughly two orders of magnitude smaller than the size of the cells, that practically all of the radiative cooling of the ascending gas takes place. Thus, the temperature excess of the ascending gas is lost in this layer, not because the stratification turns from unstable to stable, but because of very efficient radiative energy transport (the change in entropy stratification is a result of the changing temperature fluctuations, rather than the other way around).

2.3. Penetrative boundaries

The further penetration of convective motions into a stable layer implies a tendency for a correlation between ascending motion and *negative* temperature fluctuations. But both the temperature stratification and the horizontal temperature fluctuations are strongly influenced by radiative transfer effects throughout the photosphere, with a significant radiative heating of the upper layers of the photosphere, relative to the adiabatic stratification that would otherwise result from the penetrative convection. For example, over a height interval where the pressure drops by two orders magnitude, the adiabatic temperature drop of an ideal gas would be about a factor of 6, whereas in the solar photosphere the mean temperature only drops by a factor of less than 1.5.

Thus, we are actually observing the overshoot of cells that are an order of magnitude larger than the local scale height; these cells are loosing their excess thermal energy in a layer that is again an order of magnitude smaller than the local scale height, and are then overshooting into a stable layer where the energetics are dominated by non-local radiative transfer.

Under these conditions, it is entirely futile to apply analytical theories (Canuto & Mazitelli 1991, 1992) that take account of neither the strong stratification, nor of the

rapid cooling of excess heat at the surface, nor of the radiative heating in the transparent photosphere.

Such theories are equally inapplicable below the optical surface, where the stratification changes towards adiabatic over an interval in depth an order of magnitude smaller than the size of cells. The entropy of a fluid parcel in this layer (and by implication its contribution to the buoyancy driving) obviously depends on the history of the fluid parcel more than on the local properties in the layer. Thus, the structure of this transition layer—which is crucial for the reflection properties of p-modes—is determined by a complex non-local average, that includes a significant influence from the radiatively dominated surface layers.

Numerical simulations, on the other hand, are capable of handling all these complications, provided the necessary level of detail is included in the numerical model. Thus, in order to adequately describe the surface boundary layer, it is necessary to adopt an equation of state that takes into account the influence of atomic ionization and molecular dissociation. An adequate description of the radiative energy transfer requires: 1) a calculation of the corresponding continuum opacity, 2) at least a statistical description of the thousands of spectral lines that contribute to the energy balance in the photosphere, and 3) a solution of the three-dimensional radiative transfer equations for every time step of the simulations, to provide the instantaneous cooling or heating of the gas by the radiation field.

The main limitation of numerical simulations is their numerical resolution; it is not possible to cover the huge range in spatial and temporal scales represented in the solar convection zone in a single numerical model. Somewhat paradoxically, it is easier to make realistic and accurate models of the violent surface layers than to model the relatively benign motions in the bulk of the convection zone. The reason is basically the requirement on the range of scales covered.

A model of the bulk of the convection zone cannot include the surface boundary layer, since that would imply simultaneous handling of time scales and spatial scales covering many orders of magnitude. Furthermore, unless one invokes an approximation that filters out sound waves and internal gravity waves, one has a serious problem with the ratio of turn-over time to wave travel times across the model.

In the remainder of this article we describe the surface region and the rest of the convection zone separately, and we stress at this point that the models of the surface region are realistic to the point that quantitative comparisons with observations can be made (and indeed show very good agreement), whereas the models of the bulk of the convection zone should be regarded as "toy models", the purpose of which are only to serve as a basis for a discussion of generic properties of these layers.

3. The surface boundary layer

Fig. 3 shows a perspective view of the surface layers of the solar convection zone. Several key properties of the surface layers are immediately obvious in this illustration: 1) The very sharp transition at the surface. The depth interval over which most of the entropy drop occurs is only 10–20 km; i.e., only abut 1% of the size of the convection cells visible at the surface. 2) The cellular structure at the surface, visualized here as actual
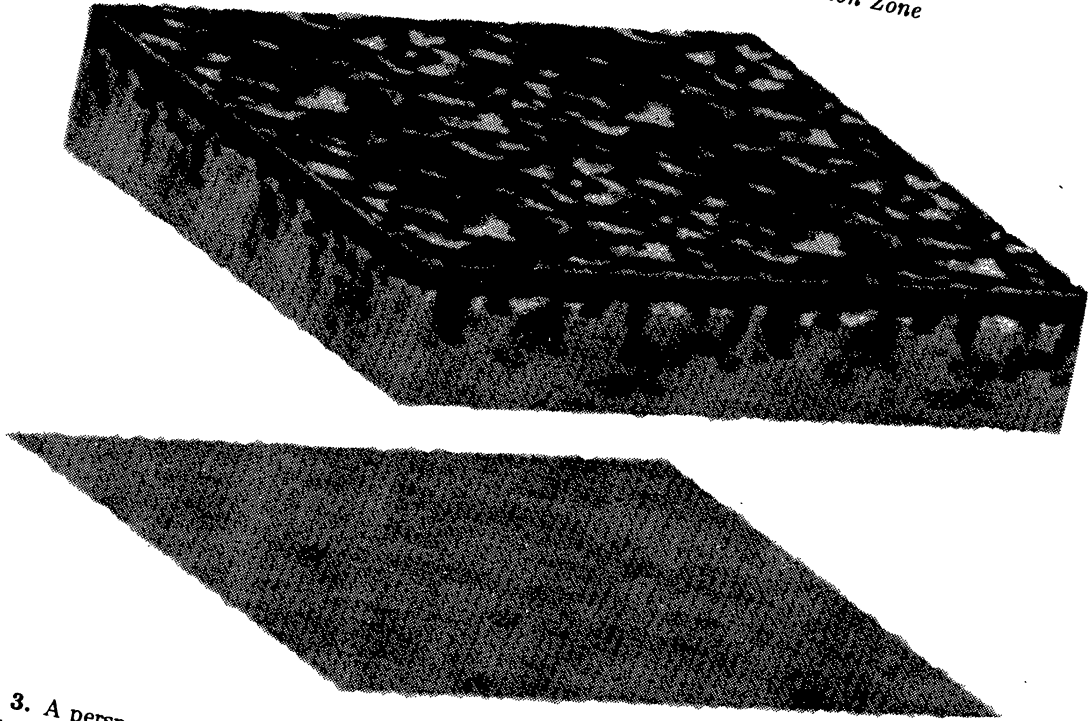
Figure 3. A perspective view of the top boundary layer of the solar convection zone. The top surface shows the optical surface brightness in a 12 × 12 × 9 Mm model of solar surface convection (Stein & Nordlund 1996), replicated in a 2 × 2 patter horizontally for clarity. The side faces, and the drop-bottom plane (a plane at a depth of 6 Mm) shows the entropy. The weak larger scale pattern that may be discernible in the bottom plane is caused by larger scale (meso-granulation) flows that are not immediately visible at the surface).

optical surface brightness. The surface brightness pattern corresponds very closely to the temperature pattern at a continuum optical depth of unity (the surface with $\tau = 1$ is significantly corrugated, because of the extreme temperature sensitivity of the opacity). 3) The filamentary downdrafts, that extend downwards from the surface, with an entropy contrast that decreases with depth because of entrainment. 4) The scale change that has occurred in the horizontal pattern, from scales of 1-2 Mm at the surface, to scales of 6-12 Mm at a depth of only 6 Mm. The scale change is a consequence of the rapid increase of scale height with depth, that allows smaller scale patterns of descending flows to merge into larger scale patterns (Stein & Nordlund 1989, Spruit et al. 1990, Spruit 1966).

3.1 Optical diagnostics

Fig. 4 shows a detailed comparison of the surface brightness patterns produced in the numerical models with high spatial resolution observations from the Swedish Solar Observatory on La Palma (Lites et al. 1989). Using an appropriate point spread function (PSF—representing the combined effects of the atmospheric seeing and the finite size of the telescope) one obtains an excellent agreement with the observations. The choice
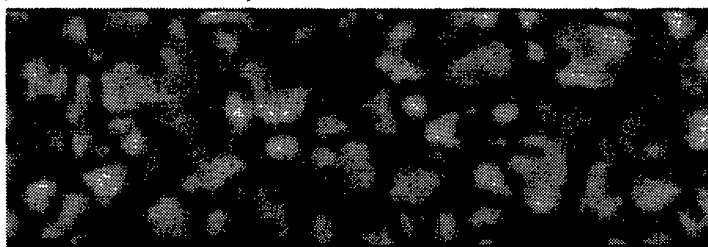
Nordlund et al.

surface brightness; 3–dimensional simulations
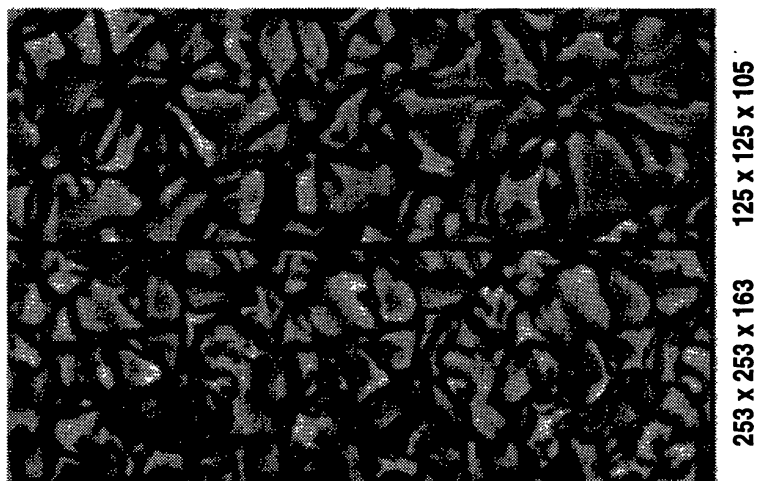
as above, simulated 40 cm telescope & atmosphere
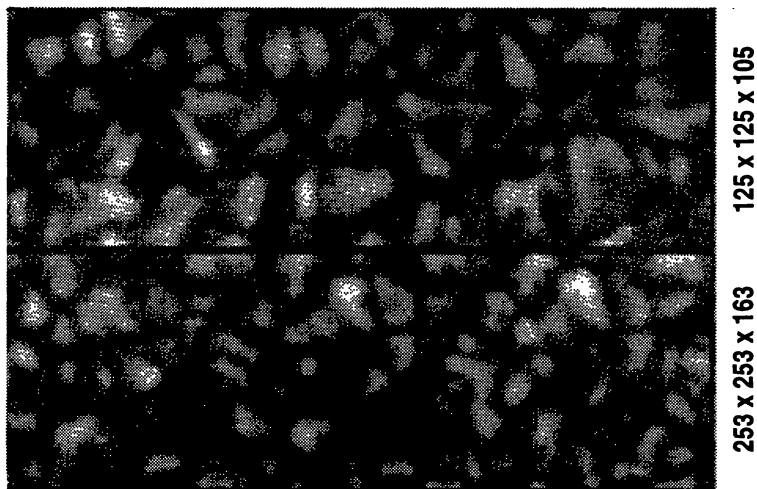
observations, Swedish 40 cm @ La Palma

Figure 4. Synthetic images from models of the solar surface boundary layer, comparing calculated surface brightness with high resolution observations from the Swedish Solar Observatory on La Palma (Lites et al. 1989). The upper two panels show the results from the models. In the middle two panels a point spread function (PSF) that represents the combined effects of the atmosphere and the instrument has been applied to the synthetic images. This PSF reduces the intensity and Doppler velocity fluctuations to the same amplitude as in the observations in the bottommost panel. The horizontal size of each panel is approximately 18 × 6 Mm.

of PSF in principle involves one free parameter; e.g., the full width at half maximum of the PSF. The correctness of the model is indicated by the fact that both the observed brightness RMS and the observed velocity RMS are reproduced with the same PSF parameters.

Independent observational constraints, that do not depend on the PSF, are provided by the width and asymmetries of spectral lines. The spectral line width is a measure of the velocity amplitude, and the spectral line asymmetry is a fingerprint that measures the correlation of velocity and brightness (temperature). An interesting indication of the robustness of the numerical results is the fact that a numerical resolution of 64^3 is sufficient to obtain good agreement with spectral line profiles (Nordlund 1982, Dravins & Nordlund 1990ab, Lites et al. 1989), while a subjective comparison of the panels in Fig. 4 shows a marginal improvement even when going from 128^2 to 253^2 horizontal resolution.

3.2 Turbulence patterns

Fig. 5 shows two volume renderings of the enstrophy density (vorticity squared, $|\nabla \times \mathbf{u}|^2$) in a snapshot from a $253 \times 253 \times 163$ simulation of the solar surface layers. The renderings each cover a small depth interval, with the rightmost panel corresponding to about 1 Mm larger depth than the leftmost panel.

As in numerical simulations of isotropic turbulence (e.g., Vincent & Meneguzzi 1994), vorticity tends to concentrate in tube-like structures, whose width are comparable to the numerical resolution of the experiment. A word of warning is in place here, however: What appears in these renderings to be classical vortex tubes are in fact structures that often have a quite different local flow topology. The peaks in vorticity, at least near the surface, are associated with the strong shear that occurs where horizontal flows are deflected downwards into the intergranular lanes. Trace particles released in the flow do not spiral around these vorticity maxima many times, as is typically the case near vortex tubes in isotropic turbulence. Rather, the trace particles display a strong shear relative to each other, and continue along with the flow, down into the intergranular lanes.

The distinction lies in the relative importance of vortical and straining motion. For a linear, incompressible flow, the topology changes from a closed circular motion, through closed elliptical motion, and over to open, straining motion, as the ratio of strain to vorticity is increased.

In addition to illustrating how the vorticity is concentrated into a cellular pattern (that we know is associated with the lanes of downdraft at the surface), Fig. 5 also illustrates that the horizontal scale of this pattern increases rapidly with depth. This increase in scale occurs because the smaller scale patterns are carried along in larger scale cellular patterns, and merge in the lanes of these larger scale cells (cf. Stein & Nordlund 1989, Spruit et al. 1990).

4. The Bulk of the CZ and the Bottom Boundary Layer

In order to begin to address questions related to the lower boundary of the solar CZ, we have constructed "toy models" of the bulk of the solar convection zone, and the bottom boundary layer (Nordlund et al. 1996). The model is cartesian, with constant acceleration

Nordlund et al.
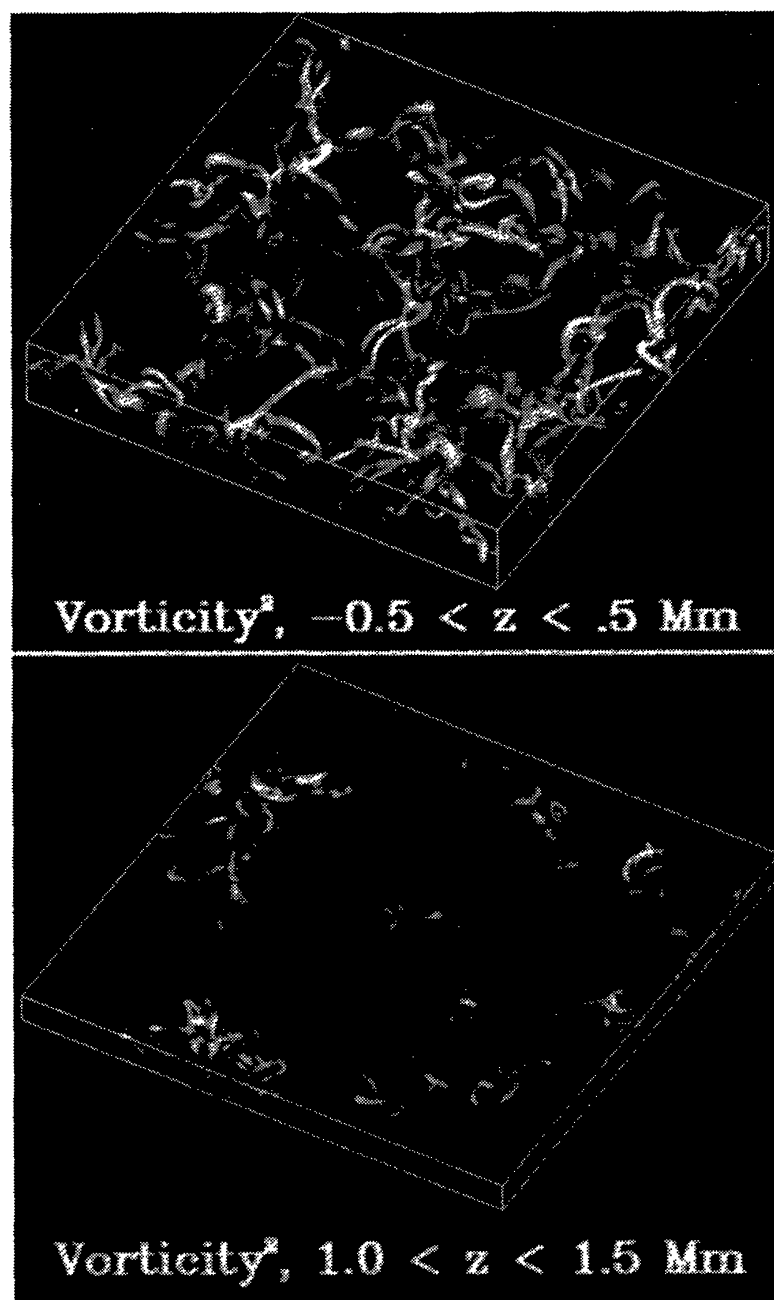
Figure 5. Volume renderings of the enstrophy density (vorticity squared, $|\nabla \times u|^2$) in a snapshot from a $253 \times 253 \times 163$ simulation of the solar surface layers, over the depth intervals indicated on the panels.

of gravity, and with linear sizes $400 \times 400 \times 300$ Mm. In order to circumvent the time step constraints associated with running compressible simulations with very small Mach numbers, we choose an average energy flux (i.e., luminosity) much larger than the solar one. Models have been run with energy fluxes between 10^6 and 10^7 times solar values, corresponding to rms Mach numbers of a few percent in most of the convection zone.

Apart from boundary effects (discussed in more detail below), the velocities in the

model scale as the cube root of the energy flux (this follows from a dimensional analysis), and the model velocities are thus at least a factor of a hundred larger than the real ones. Nevertheless, the qualitative behavior of the motions should be similar to those in the Sun. As we scale the luminosity up or down, the amplitudes of the motions change, but the patterns do not.

We use a similarly scaled Kramer's opacity law to calculate the radiative diffusion in the model, to obtain approximate balance between the radiative diffusion in the stable layer below the convection zone with the exaggerated convective flux in the convection zone. Indeed, the position of the lower boundary of the convection zone is determined by the requirement that the radiative flux at that point is sufficient to carry the entire energy flux. Above that point, the temperature gradient is essentially locked to the adiabatic value, because of the high efficiency of the convection. Thus, the radiative luminosity tapers off in proportion to the increasing value of the Kramer's opacity, just as in the solar convection zone. The convective luminosity adjusts itself, by slight adjustments of the thermal structure, until the total luminosity is independent of depth, on the average.

The thermal structure in the bulk of the convection zone is thus qualitatively similar to that in the Sun, because neither the magnitude of the convective flux nor the velocity amplitude enters into the argument above.

Since the model velocities are about a factor of one hundred larger than in the Sun, the undershoot at the bottom of the convection zone is strongly exaggerated. However, apart from the extent of penetration, we expect the morphology of the flow to be qualitatively correct.

The upper boundary of the toy model consists of a fiducial layer, where a Newtonian type cooling is applied. This creates a stable boundary layer, where ascending flow is cooled, turns over, and starts descending with an appropriate deficiency in entropy. The parameters of the cooling layer (average temperature T_0 and Newtonian cooling time τ_{cool}) are adjusted until the cooling is sufficient to sustain, on the average, the right amount of convective flux in the bulk of the convection zone. The cooling in the fiducial layer generates a cellular thermal pattern there, for basically the same reasons as at the solar surface; overturning cooling fluid collects in lanes between overturning cells. Below the "surface", the lanes break into descending cool filaments, and these again merge on larger scales.

The fiducial layer is placed at a depth where the scale height is sufficiently large for the largest scale motions to be barely resolved by the numerical mesh. There is no point in trying to place the surface higher than that, because the motions would not be resolved (and the vertical direction would be severely under-resolved). On the other hand, it is sub-optimal to place the boundary layer further down, where the motions are adequately resolved, because one should expect the first few scale heights near the boundary to be influenced by the presence of the boundary. Sufficiently far away from the boundary, the descending gas has contracted several times, and the cellular downdrafts generated at the surface have merged into filamentary downdrafts.

It is instructive to consider what happens if the surface cooling is suddenly turned off. Then the overturning flow at the surface remains isentropic, and the descending flow starts out without any entropy deficiency. Consequently, the convective flux is only non-zero as long as some of the entropy deficient material from earlier remains in the
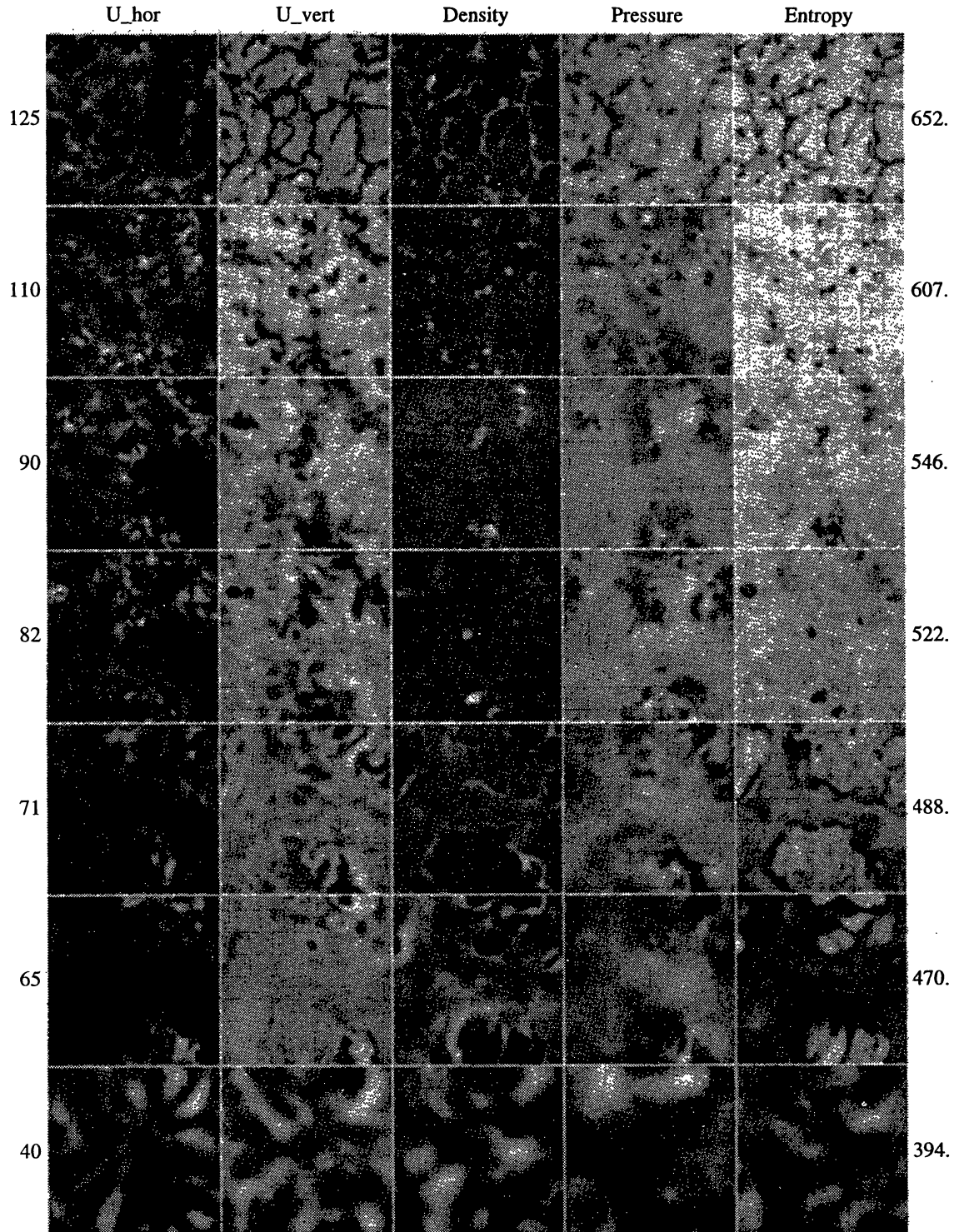
Entropy
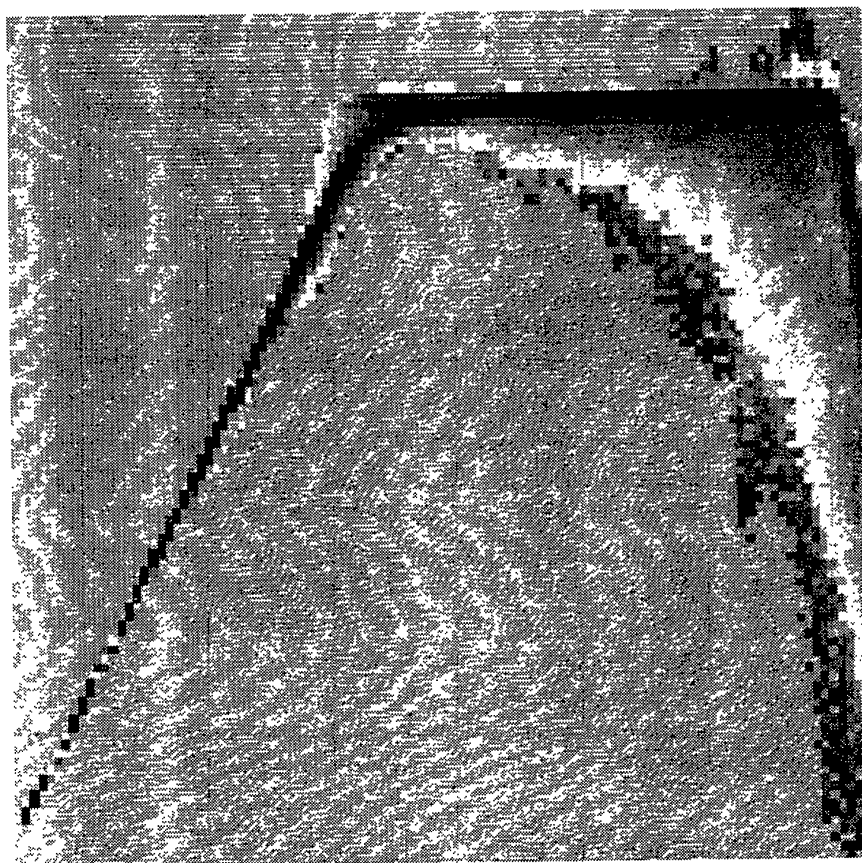
Height

Figure 6. A two-dimensional histogram of entropy, from a "toy model" of the bulk of the solar convecting zone. Each pixel column is the probability distribution function (PDF) of entropy at given radius, normalized to the same maximum at each depth (a color version of the present paper is available at URL http://www.astro.ku.dk/~aake/papers/bombay.ps.gz)

model. The convective flux thus shuts off, on a time scale equal to the time it takes for cool fluid to descend through the convection zone. A flux imbalance develops near the bottom of the CZ, and the model temperature starts to increase monotonically. A convective flux can be maintained only as long as the temperature keeps increasing, since there is no cooling at the upper boundary.

In the remainder of this Section, we show some qualitative properties of models in approximate thermal equilibrium; i.e., where the cooling in the fiducial surface layer is adequate to maintain an equilibrium.

4.1 Entrainment, entropy contrast

Fig. 6 shows a two-dimensional histogram of entropy fluctuations. For each depth, the image darkness corresponds to the relative probability of finding that particular entropy value. The figure illustrates how the entropy contrast diminishes with depth. The reason

Figure 7. The horizontal velocity, vertical velocity, density, pressure and entropy in 7 horizontal planes of the toy CZ model (resolution 128 × 128 × 136). In each panel, the quantity is scaled to the full range of a linear gray scale (the printing process may distort the linearity, though). The numbers to the right of the panels are approximate radii in Mm (the numbers to the left are depth indices).

is that overturning, nearly isentropic fluid mixes with the descending fluid, and hence the entropy deficiency of the descending fluid is diluted. In the numerical model, this occurs simply because of numerical resolution. The descending patterns of entropy deficient fluid contract (cf. Eq. (3)) until they are are at the resolution limit. Numerical diffusion prevents the patterns from shrinking further, and thus the width of the features remain about the same, but the amplitudes decrease.
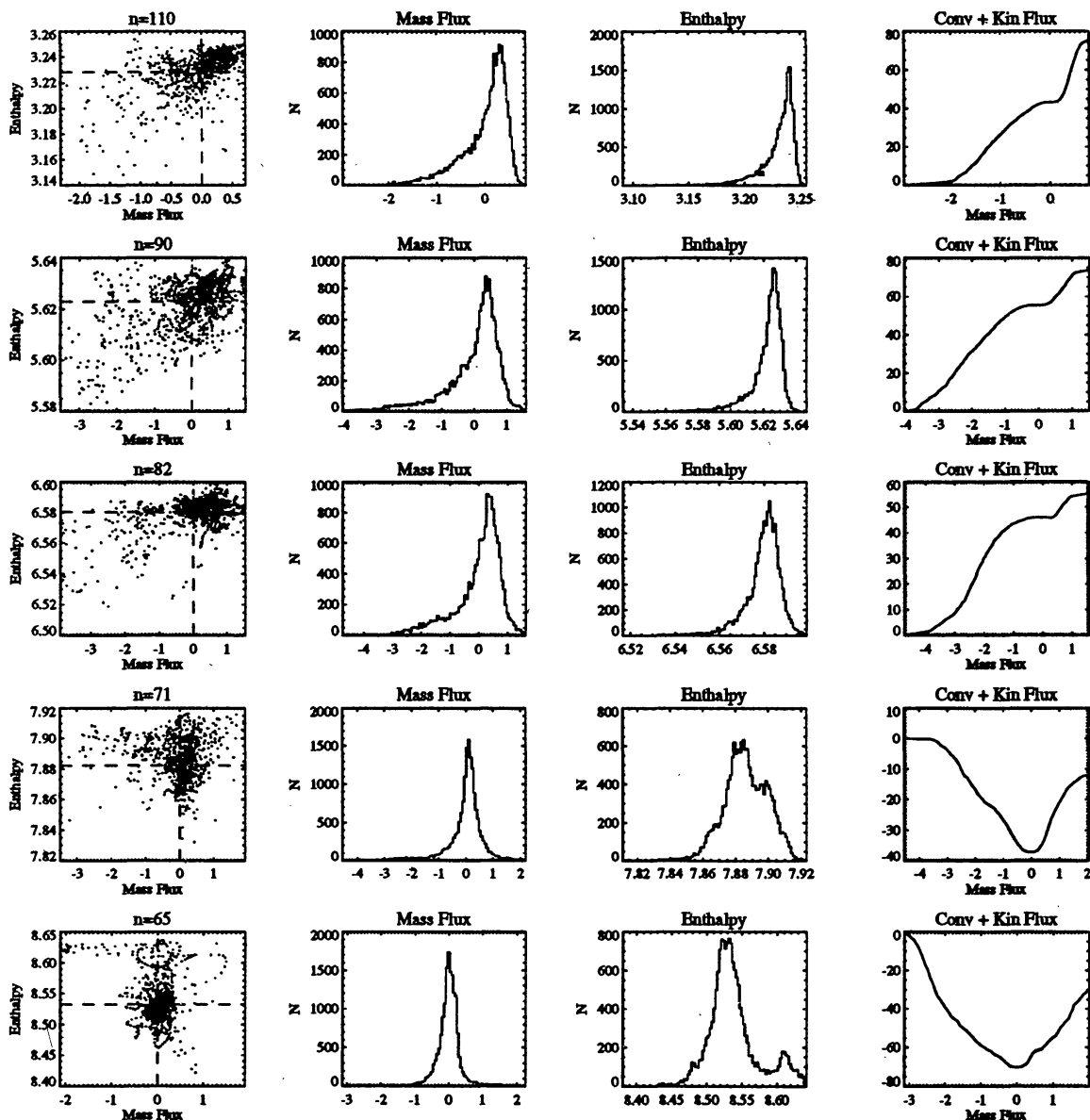
Figure 8. A montage of panels showing scatter plots of enthalpy vs. vertical mass flux, probability distribution functions for mass flux and enthalpy fluctuations, and the contributions to the convective flux, sorted by vertical mass flux.

The image mosaic in Fig. 7 shows key quantities in horizontal planes at various signif-

icant depths in the toy model. The top panel row lies at the interface between the surface cooling layer and the bulk of the convection zone. The horizontal patterns are cellular, and are dominated by boundary effects. The second panel row lies inside the bulk of the convection zone, about 50 Mm from the cooling layer. At this depth the downdraft lanes from the first panel row have broken up into an intermittent distribution of cool filaments. The third panel and fourth panel rows lie inside the "radiative heating layer", below the point where the average entropy has a shallow peak. At these depths, the downdrafts have merged into just a few, dominating ones. The fifth panel row lies right at the lower boundary of the convection zone, where the correlation between vertical velocity and temperature has become confused by temperature fluctuations associated with the return flows from the few dominant downdrafts. The sixth panel row lies in the undershoot region, where penetrating fluid is, on the average, hotter than the average. Finally, the seventh row lies within the wave region, where the penetration has caused the generation of an ensemble of of waves.

## 4.2 Convective and kinetic energy flux contributions

The montage of panels in Fig. 8 shows the contributions to the convective and kinetic energy flux in a number of horizontal layers. For each layer, a scatter plot illustrates the correlation between vertical mass flux and enthalpy, and the probability distribution functions of vertical mass flux and of enthalpy plus kinetic energy are shown. In the rightmost column, the accumulated convective and kinetic energy fluxes are shown as a sum over individual mesh contributions, sorted according to the vertical masss flux. The figures illustrates the strong skewness of the probability distribution functions that corresponds to the intermittency of the downdrafts in the bulk of the convection zone. The ratio between the fractional flux carried by updrafts and downdrafts may be read off the rightmost column of panels, where the part due to the downdraft corresonds to the values of the functions at zero vertical mass flux. The part corresponding to the ascending flow is the remaining change out to the rightmost boundary of the plot.

Fig. 9 shows the horizontally averaged convective flux, as a function of depth and time. The constancy of the convective flux with time shows that the model is thermally relaxed. Note the gradual increase of the convective flux above the bottom of the convection zone, corresponding to the gradual decrease of the radiative flux associated with the increase of the Kramer's opacity. The fluctuations in the convection zone are mainly caused by descending filaments of cool fluid, while the fluctuations *below* the convection zone are mostly associated with g-mode type motions there.

Fig. 10 shows the mean structure of the CZ toy model. We discern the following layers, from the top towards the bottom:

1) At the very top, there is a layer where the temperature gradient is significantly higher than the adiabatic value (0.4). This is a signature of the fiducial cooling layer, where the ascending gas is cooled, turns over and starts to descend.

2) Through the upper parts of the convection zone, the temperature gradient is close to the adiabatic value, and the luminosity is carried almost entirely by convection (with the convective flux being larger than the luminosity to compensate for the downward directed kinetic energy flux). This is the "bulk of the convection zone".
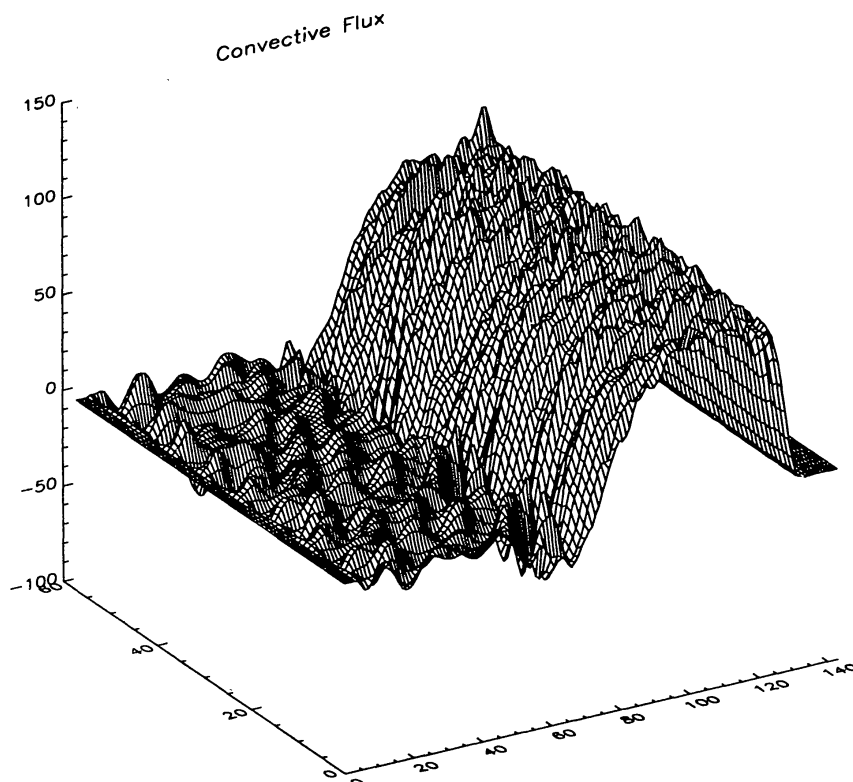
Figure 9. Surface plot of $F_{conv}(r/R, t)$, where radius increases to the right, and time increases to the left.

3) As the radiative flux starts to become noticeable, the convective flux is correspondingly reduced. Throughout this region, there is a negative divergence of radiative flux; i.e., the fluid is being heated on the average. We refer to this region as the "radiative heating region". Since the radiative flux is almost uniformly distributed in horizontal planes, most of the heating goes into the almost uniform ascending flow, whose entropy thus increases slowly with height. The entropy of the descending flow increases with depth, both because of the entrainment and because of the radiative heating. Thus the entropy contrast between the descending and ascending fluid decreases with depth, and there may be patches of descending fluid that actually have a higher entropy than the average (while still lower than the entropy of the ascending fluid).

4) Eventually, a point is reached where the convective flux on the average vanishes. We define this to be the "bottom of the convection zone". Depending on whether one includes the kinetic energy flux or not, the exact position varies slightly. Below this point, descending fluid has, even on the average, a higher entropy than the average, and hence experiences buoyancy braking. As a consequence, the narrow downdrafts "splat out", the descent is rapidly stopped, the fluid overturns and starts to ascend. We denote this region the "undershoot layer". Depending on the vertical momentum of the downdraft when it reaches the undershoot layer, it penetrates a varying distance. Hence, independent of
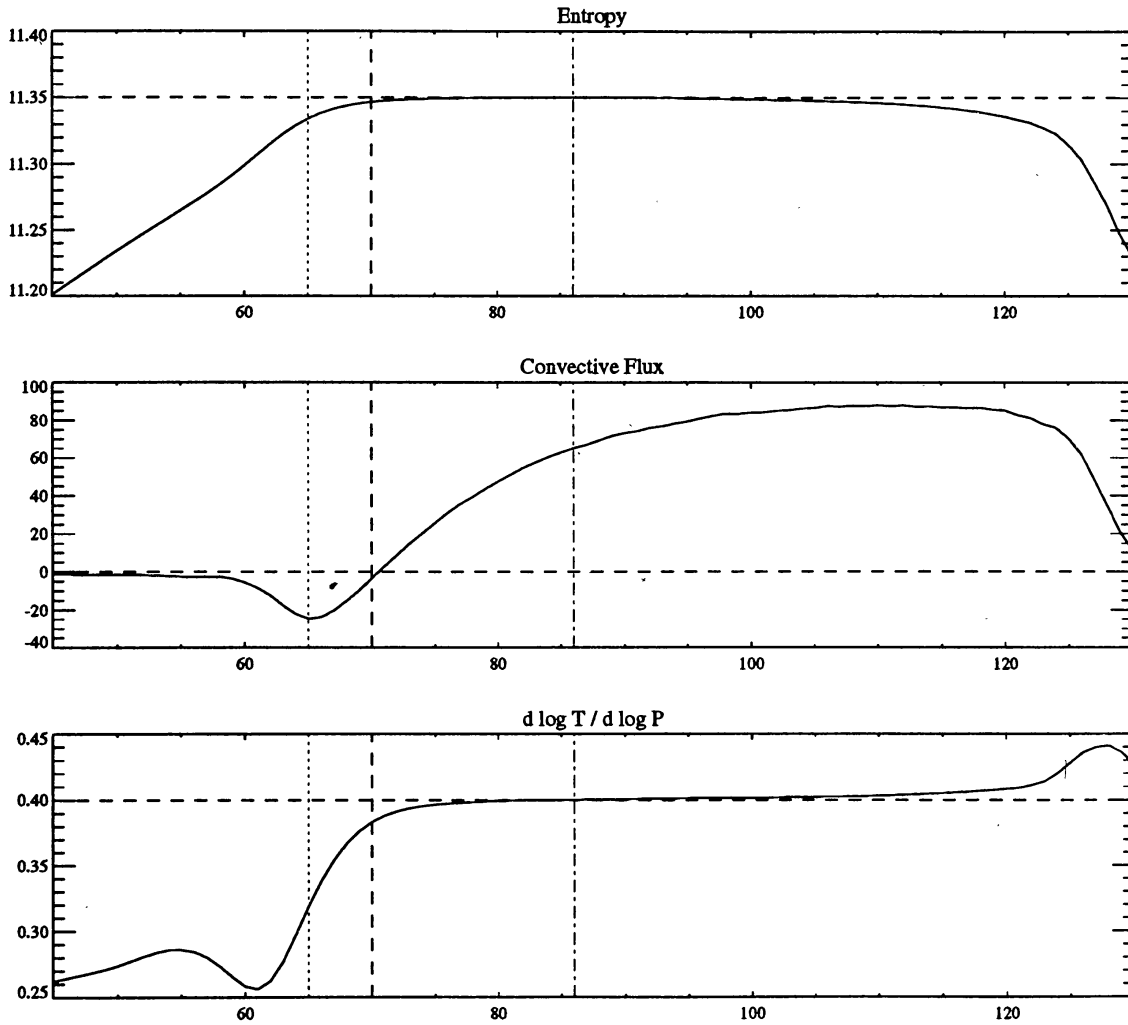
Figure 10. The mean structure of the convection zone in the toy model. The three panels show the entropy, the convective flux, and the logarithmic temperature gradient.

how abruptly the influence of an individual downdraft stops, the mean entropy profile does not develop sharp corners, because it reflects the ensemble average of a number of downdrafts with varying penetration power.

5) Below the undershoot layer, there is a stable layer into which the downdrafts do not penetrate, in the sense that there is no direct fluid exchange with the convection zone. However, wave like motions are excited in this region, by the pressure fluctuations associated with the penetrating downdrafts, and we thus refer to this region as the "wave region". To obey the continuity equation, each downdraft must induce a pressure fluctuation ahead of itself. This pressure fluctuation matches smoothly onto a wave-like solution below the undershoot layer. Thus, each penetrating downdraft excites motions in the wave region, and the ensemble of penetrating downdrafts maintain a spectrum of wave motions there. Throughout the wave region, the energy density of the waves

is approximately constant (or, to be more precise, is approximately constant per unit acoustic optical depth).

Each penetrating downdraft has, associated with it, a particular solution of the linearized fluid equations, with exponential vertical behavior, and sinusoidal horizontal behavior; this follows from the solution of the Laplace equation for the pressure, in a convectively stable region; c.f. Nordlund (1982) and Freytag et al. (1996). This vertically exponential behavior is probably crucial to the diffusion in the wave region, since the pure wave motions associated with the general solution of the linearized fluid equations do not produce any scalar transport, on the average. The exponential part, on the other hand, is a decaying image of the overturning motion of the downdraft head, and should contribute to transport of a scalar. The consequences of such a picture for Li diffusion are worked out by Freytag et al. in a recent paper (1996).

5. Concluding remarks

The level of detailed agreement with observations for models of the surface boundary layer indicates that these models are adequately resolved. Different diagnostics require different amounts of numerical resolution; properties such as the mean thermal stratification are essentially converged already at horizontal resolutions of $\Delta x \approx 100$ km, while obtaining realistic details at scales comparable to the best observations requires $\Delta x \approx$ 25–50 km. It is a common property of even the best numerical codes that wavenumbers larger than about $k_{\text{Nyquist}}/5$ have too little power; this simply reflects the necessity of having adequate dissipation at the smallest scales. In the case of the solar surface boundary layer, these scales carry little energy even in resolved cases, which explains why the thermal stratification and other integral properties do not require particularly high numerical resolution.

We thus conclude that current numerical models of the solar surface layers are quite robust, and that they may be applied with confidence to such questions as the detailed reflection properties of p-modes at the solar surface. Provided that consistent equations of state are used, one should be able to directly compare the wave propagation in the three-dimensional models with that in one-dimensional mean models.

The difference between "standard" one-dimensional models of the solar surface layers, using either classical mixing length theory, or some more recent variants thereof (Canuto & Mazitelli 1991), and three-dimensional models may be divided into two parts: 1) The difference between the mean models. There may even be some ambiguity involved in making such comparisons, because it is not always clear how to best define horizontal averages in 3-D models with large amplitude horizontal fluctuations (Rosenthal et al. 1996). 2) The difference in wave propagation properties between the mean model, and the actual 3-D model, where the wave fronts are subject to the actual fluctuating quantities, rather than to their horizontal means. The latter difference includes the effects of non-adiabaticity; e.g., the effects of fluctuations in the radiation field.

Models of the deeper layers of the solar convection zone have not yet reached the sophistication of the surface models. However, a number of properties of the "toy models" are generic, and should not depend much on the details of the model. Thus, the behavior of the downdrafts below the surface, where they merge on larger and larger scales, should

be generic, and independent of the numerical resolution. It, as well as the reduction of entropy contrast due to entrainment, depends only on the density stratification, which forces most of the ascending flow to overturn within a density scale height. Likewise, the behavior of the mean radiative flux, and the corresponding behavior of the mean entropy gradient, in the "radiative heating region" above the lower CZ boundary is also generic, since it depends only on the functional behavior of the Kramer's opacity. The gradual radiative heating leads to an extended weakly subadiabatic region in the lower parts of the convection zone, with a shallow maximum of the average entropy occurring well inside the convection zone. The numerical models also make it abundantly clear that the transition to the radiative interior cannot contain any sharp "corners" in the mean, since it is an ensemble average over downdrafts with varying penetration distances.

A lot remains to be done before models of the lower boundary layer reach the level of quantitative realism that has been obtained for the surface boundary layer. It will be necessary, either to filter out the shorter time scales, such that sufficiently slow motions and long time scales may be studied, or to learn how to scale the results obtained at much too large luminosity towards the actual solar values. Also, the interaction with differential rotation, and with dynamo magnetic field near the bottom boundary layer should be studied, in order to better understand the mechanisms behind the solar dynamo.

Acknowledgments

References

Canuto, V.M., & Mazzitelli, I. 1991, ApJ 370, 295

Canuto, V.M., & Mazzitelli, I. 1992, ApJ ???, ???

Dravins, D. & Nordlund, Å. 1990a, Astron. Astrophys., 228, 184

Dravins, D. & Nordlund, Å. 1990b, Astron. Astrophys., 228, 203

Freytag, B., Ludwig, H.-G. & Steffen, M. 1996, Astron. Astrophys. (submitted)

Lites, B.W., Nordlund, Å. & Scharmer, G. S. 1989, in *Constraints Imposed by Very High Resolution Spectra and Images on Theoretical Simulations of Granular Convection*, Solar and Stellar Granulation, eds. R.J. Rutten and G. Severino, Kluwer Academic Press

Nordlund, Å. 1982, Astron. Astrophys., 107, 1

Rosenthal, C.S., Christensen-Dalsgaard, J., Nordlund, Å., Stein, R.F., Trampedach, R. 1996, Astron. Astrophys. (to be submitted)

Spruit, H.C., Nordlund, Å. & Title, A. 1990, Annual Reviews of Astronomy and Astrophysics, 28, 263

Spruit, H. 1996, invited review at Capodimonti, Naples

Stein, R.F. & Nordlund, Å 1996 (in preparation)

Stein, R.F. & Nordlund, Å 1989, ApJ, 342, L95

Vincent, A. & Meneguzzi, M. 1994, J. Fl. Mech, 225, 1